Research Square

Preprints are preliminary reports that have not undergone peer review.
They should not be considered conclusive, used to inform clinical practice,
or referenced by the media as validated information.

Continuous and sustainable multicarbon acids electrosynthesis

Zhongshuo Zhang
University of Science and Technology of China
Yuying Zhao
University of Science and Technology of China
Zhenhao Wang
Beijing University of Chemical Technology
Jieshan Qiu
Beijing University of Chemical Technology
Ifan E. L. Stephens
Imperial College London
Jie Zeng
zengj@ustc.edu.cn

University of Science and Technology of China
Shaofeng Li
shaofengli@ustc.edu.cn

University of Science and Technology of China

Research Article

Keywords:

Posted Date: November 20th, 2026

DOI: https://doi.org/10.21203/rs.3.rs-11795109/v1

License: This work is licensed under a Creative Commons Attribution 4.0 International License.
Read Full License

Additional Declarations: The authors declare no competing interests.

Continuous and sustainable multicarbon acids electrosynthesis

Zhongshuo Zhang[1,2], Yuying Zhao[2], Zhenhao Wang[1,3], Jieshan Qiu[3], Ifan E. L. Stephens[4], Jie Zeng[1,2,5,6,*], Shaofeng Li[1,*]

[1]State Key Laboratory of Precision and Intelligent Chemistry, School of Chemistry and Materials Science, University of Science and Technology of China, Hefei, Anhui 230026, P. R. China

[2]Hefei National Research Center for Physical Sciences at the Microscale, Key Laboratory of Strongly-Coupled Quantum Matter Physics of Chinese Academy of Sciences, Key Laboratory of Surface and Interface Chemistry and Energy Catalysis of Anhui Higher Education Institutes, Department of Chemical Physics, University of Science and Technology of China, Hefei, Anhui 230026, P. R. China

[3]State Key Laboratory of Chemical Resource Engineering, College of Chemical Engineering, Beijing University of Chemical Technology, Beijing 100029, P. R. China

[4]Department of Materials, Imperial College London, London SW7 2AZ, United Kingdom

[5]School of Chemistry & Chemical Engineering, Anhui University of Technology, Ma'anshan, Anhui 243002, P. R. China

[6]Deep Space Exploration Laboratory, Hefei 230088, P. R. China

*Correspondence and requests for materials should be addressed to Jie Zeng (zengj@ustc.edu.cn) and Shaofeng Li (shaofengli@ustc.edu.cn)

Abstract

Electrochemical CO_2 reduction offers a route to produce fuels and chemicals using renewable electricity. Multicarbon electrosynthesis has predominantly relied on Cu-based catalysts in aqueous electrolytes, achieving high multicarbon faradaic efficiencies but facing broad product distributions and substantial carbon loss through carbonate formation. Nonaqueous CO_2 electrolysis offers an alternative pathway to multicarbon synthesis through radical C–C coupling while suppressing carbonate formation. However, the full-cell operation remains limited by sacrificial anodic reactions and poorly controlled proton delivery. Here, we introduce a hydrogen-oxidation-enabled full-cell architecture that couples nonsacrificial anodic H_2 oxidation with continuous nonaqueous CO_2 reduction. Hydrogen oxidation provides a regulated proton flux without disrupting the low-water environment required for radical chemistry. Pairing a PtAu anode with an oxide-derived Pb cathode enables continuous conversion of CO_2 and H_2 to oxalic and glyoxylic acids, achieving a C_2 acid faradaic efficiency of 97 ± 2% at 30 milliamperes per square centimeter and a single-pass carbon utilization efficiency of 72 ± 2%. In contrast, anodic water oxidation promotes water accumulation and shifts cathodic selectivity towards hydrogen and single-carbon products. This approach establishes anodic reaction engineering as a route to continuous, carbon-efficient nonaqueous multicarbon electrosynthesis.

Introduction

Electrochemical CO_2 reduction offers a route to convert CO_2 and renewable electricity into fuels and chemicals[1-3]. Advances in catalysts and reactor design have enabled selective production of CO and formic acid with faradaic efficiencies (FEs) exceeding 90%[4-7]. Extending this control to multicarbon (C_{2+}) products is more challenging[8,9]. Formation of C–C bonds introduces additional reaction intermediates and competing pathways, making it difficult to simultaneously achieve high product selectivity and efficient carbon utilization[1,10].

Most multicarbon CO_2 electrosynthesis has been developed in aqueous electrolytes on Cu-based catalysts[10]. In this reaction paradigm, C–C bonds form primarily through coupling of surface-bound CO-derived intermediates (Fig. 1a)[11-14]. Subsequent protonation, hydrogenation, and deoxygenation generate a complex network of C_{2+} products, including olefins, alcohols, and carboxylates, even when their combined FE reaches 70 to 90%[8,9]. The aqueous environment imposes an additional limitation on carbon utilization. In neutral and alkaline electrolytes, hydroxide generated during cathodic CO_2 reduction (CO_2R) reacts with CO_2 to form carbonate, leading to substantial carbon loss and limiting the single-pass carbon utilization efficiency (SPCE) to below 25%[1,15,16]. Strategies such as carbonate recovery and acid-humidified CO_2 feeds can mitigate this carbon loss but do not eliminate the underlying carbonate equilibrium[17,18]. Acidic operation suppresses carbonate formation but increases competition from hydrogen evolution and places additional constraints on C_{2+} selectivity[15,19-21]. Thus, simultaneously controlling C–C bond formation, product distribution, and carbon utilization remains a central challenge for aqueous CO_2 electrolysis (Supplementary Table 1).

Nonaqueous CO_2 reduction offers a fundamentally different pathway to oxygen-rich multicarbon products, including oxalic and glyoxylic acids[22-26]. One-electron activation of CO_2 can generate CO_2 radical anions ($CO_2^{\bullet-}$), which couple directly to form oxalate without requiring C–C bond formation between surface-bound CO intermediates or participation in aqueous carbonate equilibria (Fig. 1b)[22,27]. This pathway directly constructs the C_2 framework from two activated CO_2 molecules while retaining much of the oxygen content of the reactant. By suppressing carbonate-associated CO_2 loss, this pathway offers a route to combine high C_2 selectivity with efficient carbon utilization (Fig. 1c). Pb, Hg, and molecular catalysts have

accordingly achieved oxalate FEs above 80% in propylene carbonate- and acetonitrile-based electrolytes (Supplementary Table 2)[22-24,28,29]. These studies established the feasibility of radical-mediated C–C coupling, but they largely relied on batch configurations, sacrificial counter electrodes, or poorly controlled proton sources. How to translate this chemistry into a continuous full-cell process therefore remains unresolved.

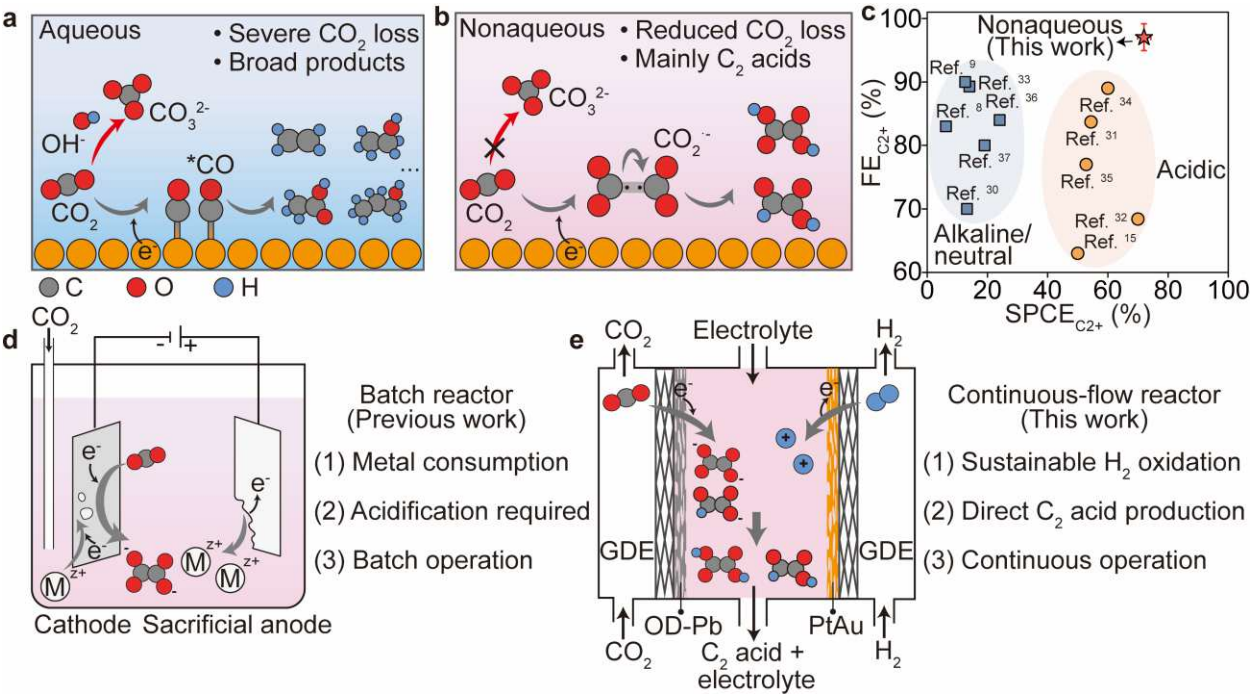


Fig. 1 Anodic reaction engineering enables continuous nonaqueous CO_2 electrolysis. a, Aqueous multicarbon CO_2 reduction through coupling of surface-bound CO-derived intermediates, accompanied by carbonate formation and a broad product distribution. **b**, Nonaqueous C–C bond formation through coupling of solution-accessible CO_2 radical anions, followed by formation of oxalic and glyoxylic acids. **c**, Comparison of C_{2+} faradaic efficiency (FE) and C_{2+} single-pass carbon utilization efficiency (SPCE) for representative alkaline or neutral, acidic, and nonaqueous CO_2 electrolysis systems[8,9,15,30-37]. The star denotes this work. Error bars indicate standard deviations from three independent experiments. **d**, Conventional nonaqueous CO_2 electrolysis using a sacrificial metal anode. **e**, Continuous-flow electrolyzer coupling CO_2 reduction on an oxide-derived Pb cathode with H_2 oxidation on a PtAu anode. GDE, gas diffusion electrode.

This transition from half-cell chemistry to continuous electrolysis shifts a critical design challenge from the cathode to the anodic reaction[26]. Oxidation of organic solvents requires high anodic potentials and accelerates electrolyte degradation (Supplementary Fig. 1), whereas sacrificial Zn or Mg anodes consume stoichiometric amounts of metal, generate metal-containing products and waste, require downstream acidification, and introduce metal contamination into the cathodic catalyst (Fig. 1d)[38-40]. Nonsacrificial anodic reactions, such as hydrogen oxidation or water oxidation, could instead sustain continuous operation. However, in nonaqueous electroreduction systems, the anodic reaction controls more than the cell voltage. It also governs the transport of protons and water to the cathodic reaction environment, thereby redirecting product selectivity[38,41-43]. This creates a fundamental challenge: proton equivalents are required to convert oxalate-derived intermediates into protonated C_2 acids, whereas excessive water disrupts the low-water environment needed to sustain radical-mediated C–C coupling. Continuous nonaqueous electrosynthesis therefore requires proton delivery to be decoupled from bulk water accumulation.

Here, we achieve this decoupling by pairing nonaqueous CO_2 reduction at an oxide-derived Pb (OD-Pb) gas diffusion cathode with hydrogen oxidation at a PtAu gas diffusion anode in a continuous-flow electrolyzer (Fig. 1e). Rather than serving only as a nonsacrificial counter reaction, hydrogen oxidation reaction (HOR) regulates the cathodic reaction environment by providing a controlled proton flux while maintaining low water content. By contrast, replacing HOR with oxygen evolution reaction (OER) causes substantial water accumulation and redirects cathodic selectivity from C_2 acids towards H_2 and C_1 products. Under the HOR-coupled operation, OD-Pb achieves a total C_2 acid FE of 97 ± 2% at 30 mA cm^{-2} (Fig. 1c), comprising 64 ± 1% oxalic acid and 33 ± 2% glyoxylic acid. Radical-trapping experiments and water-dependent controls further indicate that excessive water suppresses C–C coupling involving short-lived, solution-accessible CO_2 radical species. Avoiding carbonate-mediated carbon loss enables a single-pass carbon utilization efficiency of 72 ± 2% (Fig. 1c), while control of local CO_2 availability tunes the partitioning between oxalic and glyoxylic acids. These results establish anodic reaction engineering as a design principle for continuous, selective, and carbon-efficient nonaqueous multicarbon electrosynthesis.

Results

Cathode identity redirects CO_2 activation

We constructed a continuous-flow electrolyzer that couples nonaqueous CO_2 reduction with HOR (Fig. 2a, Supplementary Fig. 2, 3). A porous cathode positioned between a CO_2 flow channel and a circulating electrolyte delivered CO_2 directly to the electrode-electrolyte interface. The electrolyte consists of 1 M tetrabutylammonium tetrafluoroborate ($TBABF_4$) in acetonitrile, which provides high chemical stability, a broad electrochemical window, and high CO_2 solubility[44-46]. Building on our previous demonstration of HOR in organic electrolytes, we used a PtAu anode designed to mitigate adsorption of organic electrolyte species and poisoning intermediates (Supplementary Fig. 4–6)[47,48]. Gaseous and liquid products were analyzed by online mass spectrometry (MS, Supplementary Fig. 7) and high-performance liquid chromatography, respectively (Supplementary Fig. 8). Cu provides a stringent test of whether the reaction environment can sustain the surface-mediated C–C coupling chemistry characteristic of aqueous CO_2 reduction[11]. Full-range mass spectra collected at open circuit and at 20 mA cm^{-2} showed an increase at m/z = 28 during electrolysis (Supplementary Fig. 9). Gas chromatography identified this signal as CO, and no gaseous C_2 products, including ethylene, were detected (Supplementary Fig. 10).

During stepwise increases in current density from 5 to 25 mA cm^{-2} with time-resolved operando mass spectrometry, the CO signal appeared immediately after current was applied and increased with current density, whereas H_2 remained negligible (Fig. 2b). At 20 mA cm^{-2}, Cu produced CO with an FE of 88 ± 2%, while the combined FE for oxalic and glyoxylic acids was below 2% (Fig. 2c). Operando Raman spectroscopy showed no detectable accumulation of adsorbed CO (Supplementary Fig. 11), consistent with a low steady-state CO coverage under these conditions. Together, these observations indicate that the HOR-coupled nonaqueous environment does not sustain the adsorbate required for efficient multicarbon formation on Cu.

The selectivity of Cu was not determined by the cathode alone. When the same Cu cathode and electrolyte were used in a conventional batch cell with a sacrificial Zn anode, oxalate became the dominant product with a FE of 60%, whereas CO accounted for 29% FE (Supplementary Fig. 12). This reversal from predominantly C_2 formation in the Zn-coupled batch cell to predominantly

CO formation in the HOR-coupled flow cell demonstrates that the complete reaction environment can redirect CO_2 reduction on the same cathode. Among the differences between the two configurations, the HOR-coupled cell continuously supplies proton equivalents to the cathodic reaction environment. Increased proton availability could favor protonation and C–O bond cleavage of surface-associated CO_2-derived intermediates before they desorb or couple[49].

We therefore reasoned that sustaining C–C coupling under the HOR-coupled conditions would require redirecting one-electron-activated CO_2 away from rapid surface protonation and toward a radical species accessible for coupling. Metals that weakly stabilize reduced CO_2 intermediates, such as Pb, provide a potential route to this regime[22]. PbO_2 was electrodeposited onto a porous stainless-steel mesh as a reducible precursor (Supplementary Fig. 13). Under cathodic conditions, it reconstructed into a porous electrode composed predominantly of metallic Pb, which we denote oxide-derived Pb (OD-Pb, Supplementary Fig. 14–17). OD-Pb reversed the product distribution observed on Cu. Time-resolved mass spectrometry showed negligible CO and H_2 formation as the current density increased from 5 to 25 mA cm^{-2} (Fig. 2b), consistent with the full-range mass spectrometry and GC comparison between Cu and OD-Pb (Supplementary Fig. 9, 18, 19). Instead, oxalic and glyoxylic acids dominated the product distribution (Fig. 2c, Supplementary Fig. 20, 21). At 20 mA cm^{-2}, OD-Pb achieved FEs of 71 ± 1% for oxalic acid and 27 ± 2% for glyoxylic acid, corresponding to a total C_2 acid FE of 98 ± 2%. Control electrolysis under Ar showed no corresponding liquid products (Supplementary Fig. 22, 23), and $^{13}CO_2$ isotope-labeling measurements confirmed CO_2 as the carbon source for both oxalic and glyoxylic acids (Supplementary Fig. 24).

Oxalate formation in nonaqueous CO_2 reduction has been described through both solution-phase radical coupling and surface-associated pathways[27,43]. We therefore used radical trapping to distinguish between these pathways under continuous-flow conditions. We added 5,5-dimethyl-1-pyrroline *N*-oxide (DMPO) into the electrolyte, a radical-trapping reagent that intercepts solution-accessible radicals, and assessed its influence on product selectivity.

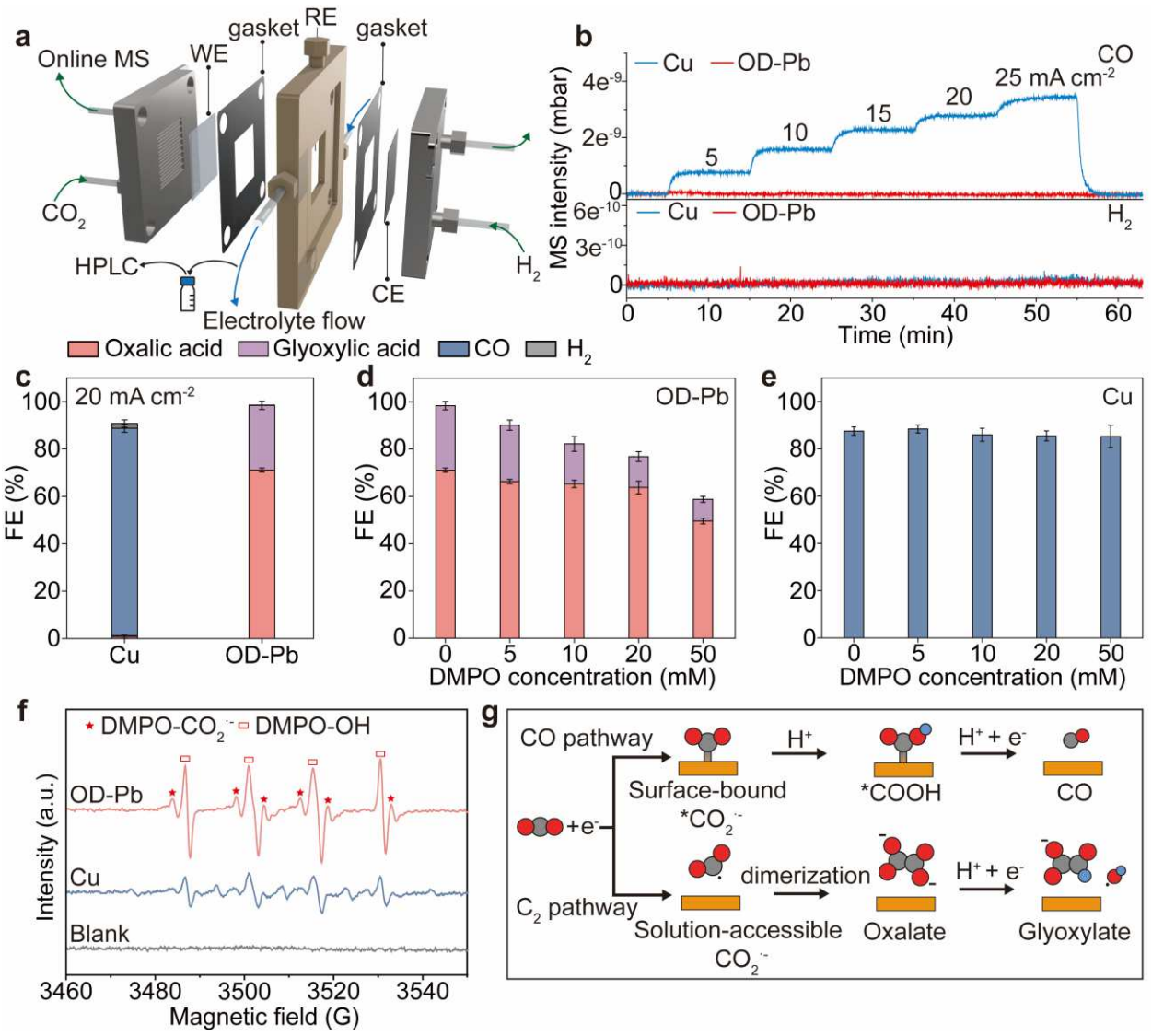


Fig. 2 Catalyst-dependent CO_2 activation pathways. a, Exploded view of the continuous-flow electrolyzer equipped with online mass spectrometry (MS). WE, working electrode; CE, counter electrode; RE, reference electrode; HPLC, high-performance liquid chromatography. **b**, Time-resolved CO and H_2 signals during stepwise increases in current density from 5 to 25 mA cm^{-2} on Cu and OD-Pb cathodes. **c**, Product FEs on Cu and OD-Pb at 20 mA cm^{-2}. **d**, **e**, FEs of oxalic acid and glyoxylic acid on OD-Pb (**d**) and FE of CO on Cu (**e**) as functions of DMPO concentration at 20 mA cm^{-2}. **f**, EPR spectra recorded during electrolysis on OD-Pb, Cu, and blank electrolyte. Symbols denote signals assigned to DMPO-$CO_2^{\bullet-}$ and DMPO-OH adducts. **g**, Proposed surface-bound CO-forming pathway on Cu and solution-accessible radical-coupling pathway on OD-Pb. Error bars indicate standard deviations from three independent experiments.

Increasing the DMPO concentration progressively decreased both oxalic and glyoxylic acid formation on OD-Pb, lowering the total C_2 acid FE from 98 ± 2% without DMPO to approximately 59 ± 2% at 50 mM DMPO (Fig. 2d). By contrast, the CO FE on Cu changed little over the same DMPO concentration range (Fig. 2e). The contrasting sensitivity to the radical trap supports the involvement of a solution-accessible radical intermediate in C_2 acid formation on OD-Pb, whereas CO formation on Cu is comparatively insensitive to interception of such species.

Electron paramagnetic resonance (EPR) spectroscopy provided complementary evidence (Fig. 2f, Supplementary Fig. 25). During electrolysis on OD-Pb, we observed a pronounced signal assigned to a DMPO-$CO_2^{\bullet-}$ adduct[50]. The corresponding signal was substantially weaker on Cu and absent from the blank experiment. Signals assigned to a DMPO-OH adduct were also observed and may reflect secondary oxygen-containing radical chemistry accompanying downstream C_2 conversion. Together, the EPR response and the concentration-dependent inhibition by DMPO support the generation of solution-accessible CO_2 radical species on OD-Pb.

The results reveal two competing fates for one-electron-activated CO_2 (Fig. 2g). On Cu under HOR-coupled conditions, the data are consistent with a surface-associated pathway in which proton and electron transfer through intermediates such as *COOH leads to C–O bond cleavage and CO release before substantial C–C coupling occurs[51]. On OD-Pb, radical trapping and EPR instead support formation of CO_2 radical species and subsequent coupling to oxalate. We propose that subsequent proton-coupled reduction converts a fraction of this C_2 intermediate to glyoxylate[23,25,52,53]. The role of Pb is therefore not to promote surface-confined C–C coupling, but to provide a weakly interacting interface that favors the release of CO_2 radical intermediates and allows radical coupling in the electrolyte phase.

Yet the above Cu cathode and Zn anode control experiments show that this catalyst-dependent picture is incomplete: changing the full-cell reaction environment reverses Cu selectivity. We therefore examined whether the anodic reaction itself could determine the fate of the cathodically generated intermediate.

The anodic environment controls the cathodic radical environment

Short-lived radical intermediates make the C_2 pathway particularly sensitive to proton availability and water content[27,43,54,55]. We therefore compared two nonsacrificial anodic reactions, i.e., HOR and OER, to determine whether changing the anode could redirect cathodic selectivity. The two cell configurations imposed distinct transport environments (Fig. 3a, b). In the CO_2R/OER cell, a proton-exchange membrane separates the nonaqueous catholyte from an aqueous anolyte (Fig. 3a). In the membrane-free CO_2R/HOR cell, CO_2 reduction and hydrogen oxidation operated in the same organic electrolyte (Fig. 3b).

OD-Pb experienced comparable cathodic potential ranges in the two configurations (Fig. 3c), indicating that large differences in cathodic driving force were not responsible for the change in product distribution. The HOR anode operated at a less positive potential than OER, and the membrane-free configuration avoided membrane-associated ionic resistance (Supplementary Fig. 26). At 20 mA cm^{-2}, replacing OER with HOR decreased the full-cell voltage from 4.56 V to 3.09 ± 0.09 V (Fig. 3d, e, Supplementary Fig. 27).

Despite similar cathodic polarization, the two anodic reactions produced markedly different cathodic selectivities. In the CO_2R/OER cell, the total C_2 acid FE increased from 31% at 10 mA cm^{-2} to 62% at 30 mA cm^{-2}, but H_2, CO and formic acid were formed throughout the investigated current-density range (Fig. 3d). In the CO_2R/HOR cell, these competing pathways were largely suppressed. The total C_2 acid FE remained above 97% at 20 to 30 mA cm^{-2}, while the combined FE for CO and H_2 remained below 2% (Fig. 3e). The similar cathodic potentials but sharply different product distributions show that the anodic reaction acts as a selectivity variable, regulating cathodic chemistry through the reaction environment rather than simply balancing charge.

We hypothesized that water transported from the aqueous OER compartment promotes proton-dependent pathways before CO_2 radical species can couple[56]. To isolate the effect of water, we added controlled amounts of water to the catholyte of the CO_2R/HOR cell (Supplementary Fig. 28). The C_2 pathway tolerated low water concentrations: the total C_2 acid FE remained 89 ± 6% at 55 mM water (Fig. 3f). Further increases progressively redirected the reaction. The C_2 acid FE decreased to 80 ± 3%, 61 ± 4% and 44 ± 3% at 110, 280, and 560 mM water, respectively, accompanied by increasing formation of CO, H_2, and formic acid (Fig. 3f, g).

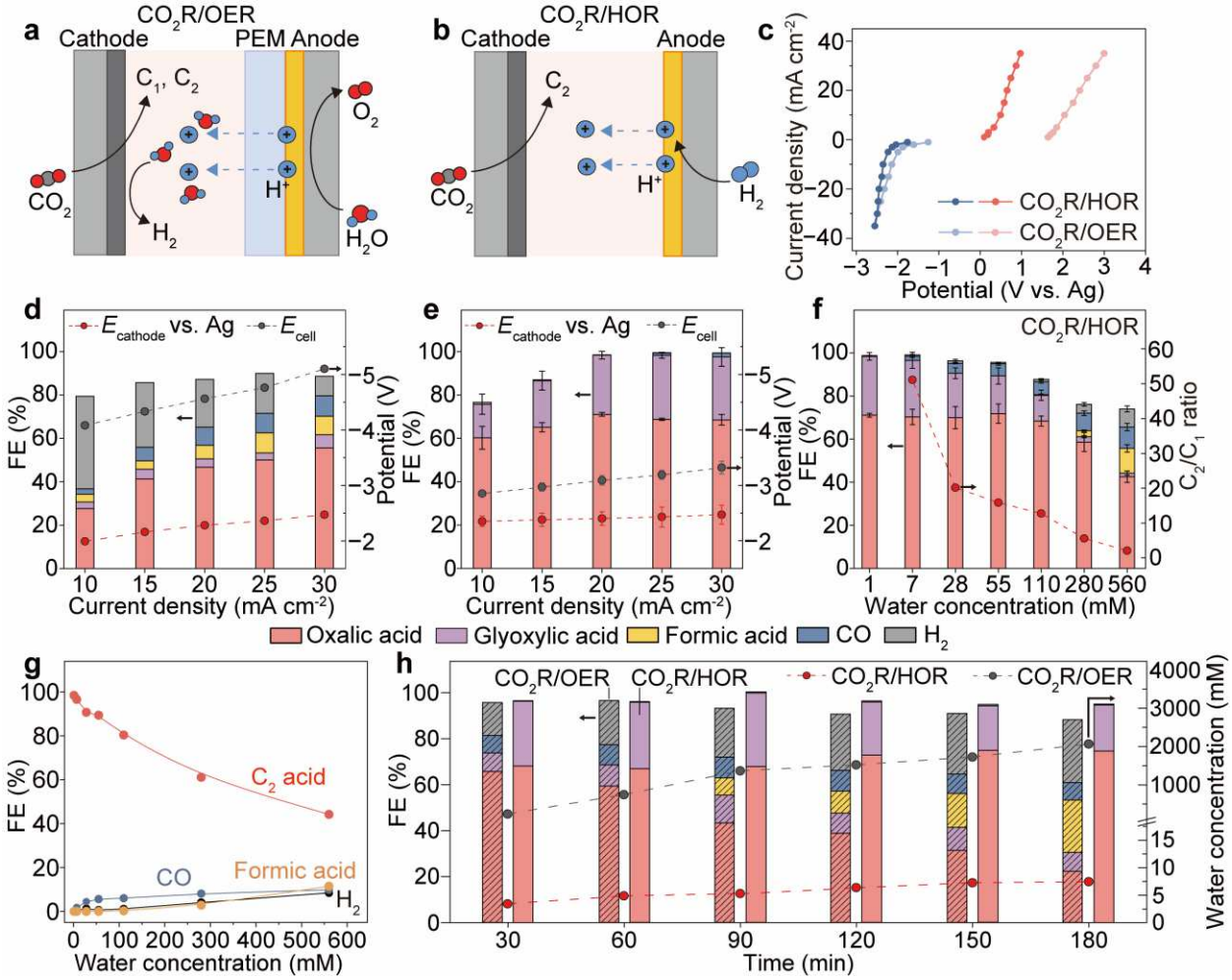


Fig. 3 Anodic reaction and water content regulate cathodic selectivity. a, **b**, Schematics of CO_2 reduction paired with OER (**a**) and HOR (**b**). The CO_2R/OER cell contains a proton-exchange membrane separating the nonaqueous catholyte from an aqueous anolyte, whereas the CO_2R/HOR cell is membrane-free. **c**, Cathodic and anodic potentials as functions of applied current density for the two configurations. **d**, **e**, Product FEs, cathodic potentials, and full-cell voltages as functions of current density in the CO_2R/OER (**d**) and CO_2R/HOR (**e**) cells. **f**, Product FEs and C_2/C_1 product ratio in the CO_2R/HOR cell as functions of catholyte water content. **g**, FEs of total C_2 acids, CO, H_2, and formic acid as functions of catholyte water content. **h**, Product FEs and catholyte water contents during continuous operation of the CO_2R/OER and CO_2R/HOR cells. The catholyte volume was 30 mL. No *iR* compensation was applied to the electrode potentials or full-cell voltages. Colors for individual products are consistent across all panels. Error bars indicate standard deviations from three independent experiments.

Water therefore changes the branching of the reaction network rather than simply suppressing CO_2 reduction. This water-dependent redistribution is consistent with previous microkinetic analyses showing that water content can strongly influence product selectivity in nonaqueous CO_2 reduction[43]. The increase in formic acid formation at high water contents further aligns with the established formate-producing behavior of Pb-based catalysts in aqueous CO_2 reduction[57]. Proton equivalents are required for downstream conversion within the C_2 sequence, including formation of glyoxylate, but high water content also promotes proton-dependent pathways that compete with coupling of CO_2 radical species. Selective C_2 formation consequently requires controlled proton delivery without excessive bulk water accumulation. The relevant design variable is therefore not proton supply alone, but the ability to decouple proton transfer from water activity.

Measurements during continuous electrolysis directly revealed the different water environments generated by the two anodic configurations. In the CO_2R/HOR cell, electrolyte water content increased only from 3 to 7 mM between 30 and 180 min, and the total C_2 acid FE remained above 90% (Fig. 3h). In the CO_2R/OER cell, water content increased from 240 mM to above 2 M over the same period, accompanied by a decline in C_2 acid FE from 74% to 30%. Passive-diffusion controls led to less than 55 mM water in the catholyte after 180 min and therefore could not account for the measured accumulation (Supplementary Fig. 29), indicating that water transport is dominated by electro-osmotic water drag accompanying hydrated proton migration rather than concentration-driven diffusion[58,59]. Because OER generates proton equivalents from water oxidation, this proton-water coupling is intrinsically linked to the anodic reaction and cannot be fully eliminated through membrane engineering.

HOR therefore does more than lower the anodic potential. It decouples proton-equivalent delivery from bulk water accumulation, preserving an environment in which CO_2 radical species can couple while downstream proton-coupled chemistry remains accessible. In this system, the anodic reaction therefore becomes an active regulator of cathodic selectivity.

Local CO_2 availability controls carbon utilization and C_2 product partitioning

Suppressing carbonate formation removes a major source of CO_2 loss in aqueous electrolysis[60]. We therefore examined whether the nonaqueous radical coupling pathway could

retain high C_2 selectivity while increasing single-pass carbon utilization. At 30 mA cm^{-2} and a total current of 187.5 mA, decreasing the pure CO_2 flow rate from 10 to 3 sccm increased the SPCE to 72 ± 2% while maintaining a total C_2 acid FE above 97% (Fig. 4a). Reducing the flow rate further to 2.4 sccm increased the SPCE to 79 ± 3%, but decreased the C_2 acid FE to 89 ± 5%. At 2 sccm, both metrics declined, to 56 ± 3% C_2 acid FE and 62 ± 3% SPCE. A CO_2 flow rate of 3 sccm therefore provided the best balance between C_2 selectivity and single-pass carbon utilization.

Changing the CO_2 supply also altered how carbon was partitioned within the C_2 pathway. As the CO_2 flow rate decreased from 10 to 3 sccm, the oxalic acid FE decreased from 64 ± 1% to 54 ± 2%, whereas the glyoxylic acid FE increased from 33 ± 2% to 43 ± 2% (Fig. 4a). The reciprocal shift suggested that CO_2 availability affects the extent of downstream conversion after C–C bond formation. We therefore changed the CO_2 partial pressure while keeping the remaining operating conditions constant (Supplementary Fig. 30). Decreasing the CO_2 content of the feed from 100% to 10% had little effect on the total C_2 acid FE but markedly redistributed the two C_2 products (Fig. 4b). The oxalic acid FE decreased from 65 ± 1% to 39 ± 2%, whereas the glyoxylic acid FE increased from 32 ± 1% to 55 ± 2% (Fig. 4b). The glyoxylic acid-to-oxalic acid ratio consequently increased from 0.5 to 1.4. The preservation of total C_2 selectivity during this redistribution suggests that decreasing CO_2 availability promotes downstream conversion within the C_2 sequence rather than primarily suppressing C–C coupling.

We next reduced the CO_2 supply under the 10% CO_2 feed to increase carbon utilization (Fig. 4c). At a CO_2 supply rate of 3 sccm, the system reached a SPCE of 62 ± 3%, a glyoxylic acid FE of 56 ± 3%, and a total C_2 acid FE of 93 ± 4%. Further reductions in CO_2 supply increased the SPCE but caused a pronounced loss of C_2 selectivity, consistent with CO_2 delivery becoming insufficient to sustain the radical-coupling pathway. Thus, dilute CO_2 feeds can retain high C_2 selectivity while shifting the product distribution toward glyoxylic acid, provided that the local CO_2 supply remains above the transport-limited regime.

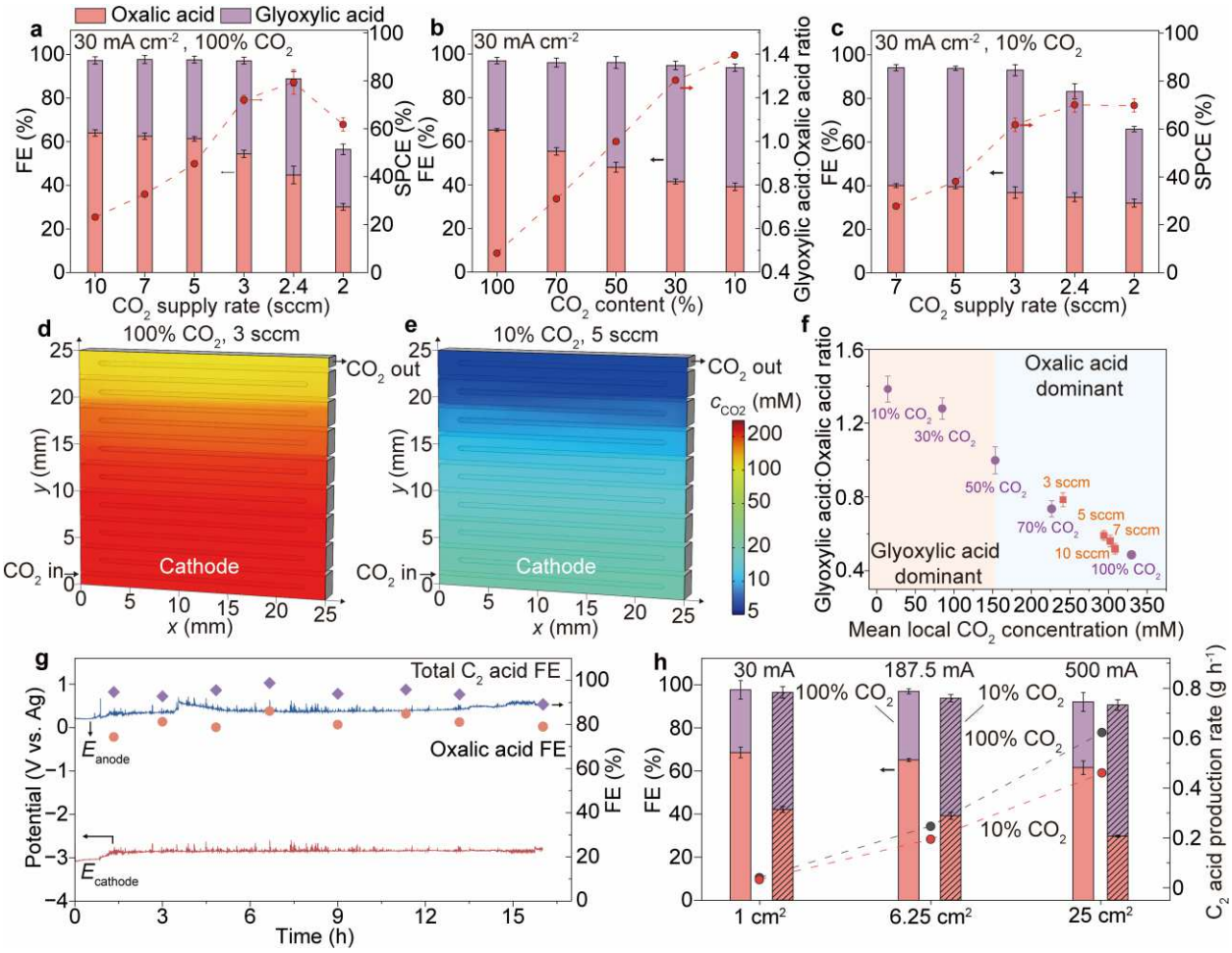


Fig. 4 CO_2 availability controls carbon utilization and C_2 product partitioning. a, FEs of oxalic and glyoxylic acids and SPCE as functions of the pure CO_2 flow rate at 30 mA cm^{-2} and a total current of 187.5 mA. **b**, FEs of oxalic and glyoxylic acids and the glyoxylic acid-to-oxalic acid ratio as functions of CO_2 content in the gas feed at 30 mA cm^{-2} and 187.5 mA. Total gas flow rate was 50 sccm. **c**, Product FEs and SPCE as functions of CO_2 supply rate using a 10% CO_2 feed at 30 mA cm^{-2} and 187.5 mA. **d**, **e**, Simulated CO_2 concentration distributions within the cathode for 100% CO_2 at 3 sccm (**d**) and 10% CO_2 at 5 sccm (**e**), respectively. **f**, Glyoxylic acid-to-oxalic acid FE ratio as a function of simulated catalyst-layer-averaged CO_2 concentration. Labels denote conditions obtained by varying pure CO_2 flow rate or CO_2 content in the feed. **g**, Continuous electrolysis at 20 mA cm^{-2} and a total current of 125 mA for 16 hours, showing cathodic and anodic potentials and FEs of total C_2 acids and oxalic acid. **h**, Product FEs and total C_2 acid production rates as the geometric electrode area increased from 1 to 6.25 and 25 cm^2 under pure and 10% CO_2 feeds. Error bars indicate standard deviations from three independent experiments.

The effects of CO_2 flow rate and feed composition raised a common question: do these external operating variables control C_2 product partitioning through the same local CO_2 environment within the catalyst layer? To address this question, we modeled CO_2 transport through the porous cathode at 30 mA cm^{-2} (Fig. 4d, e, Supplementary Fig. 31–34). The flow field and cathode geometry were defined according to the experimental electrolyzer configuration, and a 100 μm Nernst diffusion layer was introduced adjacent to the cathode surface. Lowering the pure CO_2 flow rate from 10 to 3 sccm decreased the simulated catalyst-layer-averaged CO_2 concentration from 308 to 241 mM. Changing the CO_2 fraction in the feed generated a broader concentration range, from 329 mM under pure CO_2 to 14 mM under a 10% CO_2 feed (Fig. 4f), consistent with the larger product redistribution between oxalic and glyoxylic acids observed upon feed dilution. When the experimentally measured glyoxylic acid-to-oxalic acid ratio was plotted against the simulated catalyst-layer-averaged CO_2 concentration, results obtained by independently varying flow rate and feed composition followed a common monotonic trend (Fig. 4f). The product ratio increased as the local CO_2 concentration decreased and approached unity at approximately 150 mM. This correlation indicates that local CO_2 availability, rather than flow rate or inlet composition individually, is the variable most closely associated with C_2 product partitioning.

A kinetic picture consistent with these observations is that local CO_2 availability controls the balance between upstream radical coupling and downstream C_2 reduction. Given the high CO_2 solubility in acetonitrile, which is approximately 0.35 M[44], even diluted feeds can retain sufficient dissolved CO_2 to sustain radical coupling until transport becomes limiting. At high CO_2 concentration, sustained generation of CO_2 radical species continuously replenishes oxalate through C–C coupling. As CO_2 availability decreases, the flux into this upstream pathway becomes smaller relative to the available electron and proton flux, allowing a larger fraction of the C_2 intermediate to undergo further reduction toward glyoxylate. At still lower CO_2 availability, radical generation becomes insufficient to sustain C–C coupling, and the total C_2 FE declines. Thus, catalyst-layer CO_2 concentration provides a reaction-engineering descriptor that connects gas-phase delivery to the extent of conversion within the sequential C_2 reaction network.

We next tested whether the integrated reaction environment could be sustained during extended operation. At 20 mA cm^{-2}, the electrolyzer operated continuously for 16 hours, and the total C_2 acid FE remained above 89% (Fig. 4g and Supplementary Table 3). The cathode potential remained stable, while the slight increase in anode potential could indicate the gradual deactivation of the PtAu catalyst, leading to a 6 mV h^{-1} increase in cell voltage. These measurements show that the coupled radical-generation and proton-delivery environment can be sustained beyond short electrochemical tests. We then increased the geometric electrode area from 1 to 6.25 and 25 cm^2 (Fig. 4h, Supplementary Fig. 35–37). The total C_2 acid FE remained above 90% under both pure and 10% CO_2 feeds at each electrode area. The feed-dependent product distribution was also preserved: pure CO_2 favored oxalic acid, whereas the 10% CO_2 feed shifted selectivity toward glyoxylic acid. At 25 cm^2 and a total current of 500 mA, the combined C_2 acid production rates reached 0.62 g h^{-1} under pure CO_2 and 0.46 g h^{-1} under the 10% CO_2 feed. Retention of both C_2 selectivity and feed-controlled product partitioning after a 25-fold increase in geometric area supports translation of the reaction-environment design into larger flow-electrolyzer formats.

Taken together, the results identify a set of coupled requirements for continuous nonaqueous C_2 electrosynthesis. The cathode should favor CO_2 radical species accessible to coupling; the anode should supply proton equivalents without excessive water accumulation; and CO_2 transport should be controlled to balance radical generation, carbon utilization, and downstream C_2 conversion. Coordinating these functions enables high C_2 selectivity, high single-pass carbon utilization, and tunable partitioning between oxalic and glyoxylic acids within a continuous-flow reactor.

Despite the high FE, the present system remains energetically inefficient because the nonaqueous radical pathway requires a large driving force for one-electron CO_2 activation. At 20 mA cm^{-2}, the full-cell voltage was 3.09 ± 0.09 V. A voltage-loss analysis shows that the thermodynamic potential of the $CO_2/CO_2^{\bullet-}$ couple, which has been estimated to be approximately -1.9 V to -2 V depending on the solvent environment[27,61-63], accounts for more than 60% of the total cell voltage (Supplementary Fig. 38a). The highly negative potential of this couple arises from the substantial structural reorganization required to convert linear CO_2 into the bent $CO_2^{\bullet-}$ radical anion[64]. The remaining voltage arises from *iR* drop, cathodic and anodic polarization. To evaluate the energetic performance of the system, we distinguish between a pseudo-energy

efficiency (pseudo-EE), which considers only the electrical energy supplied to the CO_2/H_2 electrolyzer, and an overall energy efficiency (EE), which additionally accounts for the energy required to produce H_2 by a water electrolyzer with 70% efficiency. Both the pseudo-EE and overall EE peaked at 20 mA cm^{-2}, reaching approximately 15.1 ± 0.4% and 9.6 ± 0.2%, respectively (Supplementary Fig. 38b). Future improvements should therefore explore alternative strategies for CO_2 activation, including surface-confined radical coupling approaches that may reduce the energetic penalty associated with freely solvated CO_2 radicals. Furthermore, developing more sustainable alternatives to Pb-based cathodes will be important.

Conclusions

We establish continuous nonaqueous multicarbon electrosynthesis by coupling CO_2 reduction on an oxide-derived Pb cathode with hydrogen oxidation on a PtAu anode as a nonsacrificial anodic reaction. Decoupling proton delivery from bulk water accumulation preserves the low-water environment that favors radical C–C coupling and enables a C_2 acid FE of 97 ± 2% with a SPCE of 72 ± 2%. Control of local CO_2 availability further tunes product partitioning between oxalic and glyoxylic acids without sacrificing overall C_2 selectivity. Continuous operation for 16 hours and scale-up to 25 cm^2 demonstrate that this integrated reaction environment can be sustained in flow-electrolyzer formats. More broadly, the results show that anodic reaction engineering can regulate cathodic intermediate fate through control of proton and water transport, providing a general design principle for nonaqueous reductive electrosynthesis.

References

1 Ozden, A. *et al.* Carbon-efficient carbon dioxide electrolysers. *Nat. Sustain.* **5**, 563-573 (2022).

2 Wang, G. *et al.* Electrocatalysis for CO_2 conversion: from fundamentals to value-added products. *Chem. Soc. Rev.* **50**, 4993-5061 (2021).

3 Cai, Y. *et al.* Self-pressurizing nanoscale capsule catalysts for CO_2 electroreduction to acetate or propanol. *Nat. Synth.* **3**, 891-902 (2024).

4 Ren, S. *et al.* Molecular electrocatalysts can mediate fast, selective CO_2 reduction in a flow cell. *Science* **365**, 367-369 (2019).

5 Li, Z. *et al.* Electro-activated indigos intensify ampere-level CO_2 reduction to CO on silver catalysts. *Nat. Commun.* **16**, 3206 (2025).

6 Lu, Q. *et al.* A selective and efficient electrocatalyst for carbon dioxide reduction. *Nat. Commun.* **5**, 3242 (2014).

7 Xia, C. *et al.* Continuous production of pure liquid fuel solutions via electrocatalytic CO_2 reduction using solid-electrolyte devices. *Nat. Energy* **4**, 776-785 (2019).

8 Garcia de Arquer, F. P. *et al.* CO_2 electrolysis to multicarbon products at activities greater than 1 A cm^{-2}. *Science* **367**, 661-666 (2020).

9 Wei, C. *et al.* A scalable, biopolymer-based microenvironment for electrochemical CO_2 conversion to multicarbon products with current densities over 2 A cm^{-2}. *Nat. Energy* **11**, 889-903 (2026).

10 Nitopi, S. *et al.* Progress and perspectives of electrochemical CO_2 reduction on copper in aqueous electrolyte. *Chem. Rev.* **119**, 7610-7672 (2019).

11 Liu, X. *et al.* pH effects on the electrochemical reduction of CO_2 towards C_2 products on stepped copper. *Nat. Commun.* **10**, 32 (2019).

12 Kortlever, R., Shen, J., Schouten, K. J. P., Calle-Vallejo, F. & Koper, M. T. Catalysts and reaction pathways for the electrochemical reduction of carbon dioxide. *J. Phys. Chem. Lett.* **6**, 4073-4082 (2015).

13 Zhang, H., Gao, J., Raciti, D. & Hall, A. S. Promoting Cu-catalysed CO_2 electroreduction to multicarbon products by tuning the activity of H_2O. *Nat. Catal.* **6**, 807-817 (2023).

14 Li, F. *et al.* Molecular tuning of CO_2-to-ethylene conversion. *Nature* **577**, 509-513 (2020).

15 Huang, J. E. *et al.* CO_2 electrolysis to multicarbon products in strong acid. *Science* **372**, 1074-1078 (2021).

16 Hao, S. *et al.* Improving the operational stability of electrochemical CO_2 reduction reaction via salt precipitation understanding and management. *Nat. Energy* **10**, 266-277 (2025).

17 Hao, S. *et al.* Acid-humidified CO_2 gas input for stable electrochemical CO_2 reduction reaction. *Science* **388**, eadr3834 (2025).

18 Kim, J. Y. T. *et al.* Recovering carbon losses in CO_2 electrolysis using a solid electrolyte reactor. *Nat. Catal.* **5**, 288-299 (2022).

19 Ling, N. *et al.* Acidic media impedes tandem catalysis reaction pathways in electrochemical CO_2 reduction. *Angew. Chem. Int. Ed.* **62**, e202308782 (2023).

20 Monteiro, M. C. *et al.* Absence of CO_2 electroreduction on copper, gold and silver electrodes without metal cations in solution. *Nat. Catal.* **4**, 654-662 (2021).

21 Gu, J. *et al.* Modulating electric field distribution by alkali cations for CO_2 electroreduction in strongly acidic medium. *Nat. Catal.* **5**, 268-276 (2022).

22 Ikeda, S., Takagi, T. & Ito, K. Selective formation of formic acid, oxalic acid, and carbon monoxide by electrochemical reduction of carbon dioxide. *Bull. Chem. Soc. Jpn.* **60**, 2517-2522 (1987).

23 Sale, H., Ubbara, G. R. & Symes, M. D. Optimising the electrochemical reduction of CO_2 to oxalic acid in propylene carbonate. *Sustain. Energy Fuels* **7**, 5093-5100 (2023).

24 Angamuthu, R., Byers, P., Lutz, M., Spek, A. L. & Bouwman, E. Electrocatalytic CO_2 conversion to oxalate by a copper complex. *Science* **327**, 313-315 (2010).

25 Sartape, R. *et al.* Nonaqueous electrochemical reactive CO_2 capture and conversion of 10% CO_2 feed to mixed carboxylic acids. *Chem. Eng. J.* **526**, 171274 (2025).

26 Longhin, F., Rodrigues Pinto, M., Elizarraras, C. I. & Seger, B. J. Insights into aprotic CO_2 electrolysis using stainless-steel gas diffusion electrodes in DMF and DMSO electrolytes. *Catal. Sci. Technol.* **16**, 6566-6580 (2026).

27 Kai, T., Zhou, M., Johnson, S., Ahn, H. S. & Bard, A. J. Direct observation of $C_2O_4^{\bullet-}$ and $CO_2^{\bullet-}$ by oxidation of oxalate within nanogap of scanning electrochemical microscope. *J. Am. Chem. Soc.* **140**, 16178-16183 (2018).

28 Jia, J. *et al.* Investigating the electrochemical reduction of CO_2 to oxalate in aprotic solvents with Pb. *ChemPhysChem* **26**, e202500136 (2025).

29 Gennaro, A. *et al.* Mechanism of the electrochemical reduction of carbon dioxide at inert electrodes in media of low proton availability. *J. Chem. Soc., Faraday Trans.* **92**, 3963-3968 (1996).

30 Zhang, G. *et al.* Efficient CO_2 electroreduction on facet-selective copper films with high conversion rate. *Nat. Commun.* **12**, 5745 (2021).

31 Ma, Z. *et al.* CO_2 electroreduction to multicarbon products in strongly acidic electrolyte via synergistically modulating the local microenvironment. *Nat. Commun.* **13**, 7596 (2022).

32 Cao, Y. *et al.* Surface hydroxide promotes CO_2 electrolysis to ethylene in acidic conditions. *Nat. Commun.* **14**, 2387 (2023).

33 Zhang, T. *et al.* Highly selective and productive reduction of carbon dioxide to multicarbon products via in situ CO management using segmented tandem electrodes. *Nat. Catal.* **5**, 202-211 (2022).

34 Xie, Y. *et al.* High carbon utilization in CO_2 reduction to multi-carbon products in acidic media. *Nat. Catal.* **5**, 564-570 (2022).

35 Feng, J. *et al.* CO_2 electrolysis to multi-carbon products in strong acid at ampere-current levels on La-Cu spheres with channels. *Nat. Commun.* **15**, 4821 (2024).

36 Subramanian, S. *et al.* CO residence time modulates multi-carbon formation rates in a zero-gap Cu based CO_2 electrolyzer. *Energy Environ. Sci.* **17**, 6728-6738 (2024).

37 He, X. *et al.* Roles of copper (I) in water-promoted CO_2 electrolysis to multi-carbon compounds. *Nat. Commun.* **15**, 9923 (2024).

38 Twilton, J. *et al.* Quinone-mediated hydrogen anode for non-aqueous reductive electrosynthesis. *Nature* **623**, 71-76 (2023).

39 Brower, R. S. *et al.* Selective electrochemical reduction of CO_2 to metal oxalates in nonaqueous solutions using trace metal Pb on carbon supports enhanced by a tailored microenvironment. *Adv. Energy Mater.* **15**, 2501286 (2025).

40 Kuzmin, J. *et al.* Borohydride oxidation as counter reaction in reductive electrosynthesis. *Angew. Chem. Int. Ed.* **64**, e202501653 (2025).

41 Ye, B. *et al.* Continuous ammonia electrosynthesis from nitrogen and water in a monolithic Pd membrane-based flow cell. *ACS Energy Lett.* **11**, 1907-1915 (2026).

42 Spry, M. *et al.* In situ spectroscopy reveals how water-driven SEI formation controls selectivity in Li-mediated N_2 reduction. *Energy Environ. Sci.* **18**, 8414-8429 (2025).

43 Bagger, A., Christensen, O., Ivanistsev, V. & Rossmeisl, J. Catalytic CO_2/CO reduction: gas, aqueous, and aprotic phases. *ACS Catal.* **12**, 2561-2568 (2022).

44 König, M., Vaes, J., Pant, D. & Klemm, E. Effect of solvents on aprotic CO_2 reduction: a study on the role of CO_2 mass transport in the product selectivity between oxalate and carbon monoxide. *J. Phys. Chem. C* **127**, 18159-18166 (2023).

45 Elgrishi, N. *et al.* A practical beginner's guide to cyclic voltammetry. *J. Chem. Educ.* **95**, 197-206 (2018).

46 Polcari, D., Dauphin-Ducharme, P. & Mauzeroll, J. Scanning electrochemical microscopy: a comprehensive review of experimental parameters from 1989 to 2015. *Chem. Rev.* **116**, 13234-13278 (2016).

47 Fu, X. *et al.* Continuous-flow electrosynthesis of ammonia by nitrogen reduction and hydrogen oxidation. *Science* **379**, 707-712 (2023).

48 Li, S. *et al.* Long-term continuous ammonia electrosynthesis. *Nature* **629**, 92-97 (2024).

49 McGregor, J.-M. *et al.* Organic electrolyte cations promote non-aqueous CO_2 reduction by mediating interfacial electric fields. *Nat. Catal.* **8**, 79-91 (2025).

50 Li, L. & Cui, C. Bulk water redox chemistry enables radical-mediated C–C coupling in CO_2 electroreduction. *Nat. Chem.* **18**, 648-655 (2026).

51 Vijay, S. *et al.* Unified mechanistic understanding of CO_2 reduction to CO on transition metal and single atom catalysts. *Nat. Catal.* **4**, 1024-1031 (2021).

52 Cheng, Y., Xu, W., Hou, J. & Kang, P. Temperature-dependent electrosynthesis of C_2 oxygenates from oxalic acid using gallium tin oxides. *ACS Catal.* **13**, 3676-3683 (2023).

53 Wang, H. *et al.* Imidazolium radical-mediated electron transfer enhances electrochemical C–N coupling for glycine synthesis. *Nat. Synth.* **5**, 74-83 (2026).

54 Kumar, A. S. *et al.* A quantitative analysis of electrochemical CO_2 reduction on copper in organic amide and nitrile-based electrolytes. *J. Phys. Chem. C* **127**, 12857-12866 (2023).

55 Deacon‐Price, C. *et al.* Influence of water content on electrochemical CO_2 reduction in acetonitrile solution on Cu electrodes. *ChemCatChem* **17**, e202401332 (2025).

56 Zawodzinski, T. A., Davey, J., Valerio, J. & Gottesfeld, S. The water content dependence of electro-osmotic drag in proton-conducting polymer electrolytes. *Electrochim. Acta* **40**, 297-302 (1995).

57 Fang, W. *et al.* Durable CO_2 conversion in the proton-exchange membrane system. *Nature* **626**, 86-91 (2024).

58 Song, J., Han, O. H. & Han, S. Nanometer-scale water- and proton-diffusion heterogeneities across water channels in polymer electrolyte membranes. *Angew. Chem. Int. Ed.* **54**, 3615-3620 (2015).

59 Janssen, G. & Overvelde, M. Water transport in the proton-exchange-membrane fuel cell: measurements of the effective drag coefficient. *J. Power Sources* **101**, 117-125 (2001).

60 Rabinowitz, J. A. & Kanan, M. W. The future of low-temperature carbon dioxide electrolysis depends on solving one basic problem. *Nat. Commun.* **11**, 5231 (2020).

61 Koppenol, W. & Rush, J. Reduction potential of the carbon dioxide/carbon dioxide radical anion: a comparison with other C_1 radicals. *J. Phys. Chem.* **91**, 4429-4430 (1987).

62 Boutin, E. *et al.* Molecular catalysis of CO_2 reduction: recent advances and perspectives in electrochemical and light-driven processes with selected Fe, Ni and Co aza macrocyclic and polypyridine complexes. *Chem. Soc. Rev.* **49**, 5772-5809 (2020).

63 Benson, E. E., Kubiak, C. P., Sathrum, A. J. & Smieja, J. M. Electrocatalytic and homogeneous approaches to conversion of CO_2 to liquid fuels. *Chem. Soc. Rev.* **38**, 89-99 (2008).

64 McNeill, A. S. & Dixon, D. A. Energetics of CO_2^- in aqueous solution. *J. Phys. Chem. A* **123**, 1243-1259 (2019).

Methods

Chemicals and materials

Tetrabutylammonium tetrafluoroborate ($TBABF_4$, Aladdin, ≥98%), acetonitrile (ACN, Aladdin, ≥99.9%), 5,5-dimethyl-1-pyrroline N-oxide (DMPO, Aladdin, ≥97%), oxalic acid dihydrate (Aladdin, ≥99%), glyoxylic acid aqueous solution (Sigma-Aldrich, 50 wt%), glycolic acid (Aladdin, ≥98%), formic acid aqueous solution (Aladdin, 10% v/v), tartaric acid (Aladdin, ≥99.5%), lead nitrate [$Pb(NO_3)_2$, Aladdin, ≥99%], copper sulfate ($CuSO_4$, Aladdin, ≥99%), $H_2PtCl_6 \cdot 6H_2O$ (Sigma-Aldrich, ACS grade), $HAuCl_4 \cdot 3H_2O$ (Sigma-Aldrich, ≥99%), and 3 Å molecular sieves (Sigma-Aldrich, 4–8 mesh beads) were used as received unless otherwise noted. High-purity CO_2, H_2, and Ar (≥99.999%) were used for electrochemical experiments and gas control measurements.

Electrode preparation

Stainless-steel and Ni mesh substrates were sequentially ultrasonicated in acetone and ultrapure water for 30 min each and dried before electrodeposition. The PbO_2 precursor was deposited onto 500-mesh stainless-steel mesh by galvanostatic anodic oxidation in 0.25 M $Pb(NO_3)_2$ and 1 M HNO_3 at 20 mA cm^{-2} for 10 min, using a graphite counter electrode. The electrode was rinsed with deionized water and dried. Before testing, the PbO_2 electrode was reconstructed into oxide-derived Pb (OD-Pb) under the standard CO_2 reduction coupled with hydrogen oxidation (CO_2R/HOR) conditions at 20 mA cm^{-2} for 1 h.

Cu cathodes were prepared by electrodeposition onto pretreated stainless-steel mesh in 0.5 M $CuSO_4$ and 1 M H_2SO_4 at a cathodic current density of 0.2 A cm^{-2} for 4 min, using a Cu-plate counter electrode. The electrodes were rinsed with deionized water and dried in an Ar-filled glovebox.

PtAu HOR anodes were prepared by hydrogen bubble-assisted electrodeposition onto 400-mesh Ni mesh following previously reported procedures[47,48]. The deposition bath contained 10 mM $H_2PtCl_6 \cdot 6H_2O$ and 10 mM $HAuCl_4 \cdot 3H_2O$ in 3 M H_2SO_4. Electrodeposition was performed at −0.1 A cm^{-2} for 3 min using a Pt-mesh counter electrode.

Electrochemical measurements

CO_2 electrolysis was performed in a custom membrane-free continuous-flow electrolyzer. The cathode and PtAu/Ni-mesh anode were positioned on opposite sides of a central electrolyte chamber, with gas-flow plates outside the electrodes (Supplementary Fig. 2, 3). The exposed geometric electrode area, defined by the flow-field gasket, was 1, 6.25 or 25 cm^2. The corresponding electrolyte volumes were 4.5, 10 and 40 mL, and the electrolyte circulation rates were 3, 10 and 30 mL min^{-1}, respectively. Electrolyte was circulated using a peristaltic pump, and Ar was supplied over the electrolyte reservoir at 10 sccm to minimize moisture ingress. Unless otherwise specified, the nonaqueous electrolyte consisted of 1.0 M $TBABF_4$ in ACN. The electrolyte was prepared in an Ar-filled glovebox (Vigor) and subsequently dried by adding 3 Å molecular sieves at 10 vol% relative to the electrolyte volume and storing overnight. After drying, the water content of the electrolyte was below 1 mM, as determined by Karl Fischer titration using an 831 KF Coulometer equipped with a 728 Stirrer (Metrohm). The electrolyte was passed through a 0.45 μm PTFE membrane filter before use.

CO_2 and H_2 were supplied to the cathode and anode gas channels, respectively, using Horiba mass flow controllers. Unless otherwise specified, both gas flow rates were 5, 10 or 30 sccm for the 1, 6.25 or 25 cm^2 cells, respectively. A 3 cm water column connected to the gas outlet maintained a small back pressure. The assembled cell was purged with CO_2 and H_2 for 10 min before electrolysis.

Measurements were performed using a BioLogic VMP2 potentiostat and an Ag-wire pseudo-reference electrode positioned near the cathode. Cathode potential, anode potential and full-cell voltage were recorded simultaneously. Electrolysis was conducted galvanostatically at ambient temperature and atmospheric pressure unless otherwise specified. No *iR* compensation was applied to all the reported potentials and cell voltages. Routine measurements used fresh electrolyte at each current density and lasted 30 min for the 1 cm^2 cell or 10 min for the 6.25 and 25 cm^2 cells. Long-term electrolysis used a 6.25 cm^2 OD-Pb cathode at 20 mA cm^{-2} (125 mA) with 900 mL electrolyte for 16 h. Liquid samples were collected at selected time points for product quantification.

Control experiments

For CO_2 reduction coupled with oxygen evolution (CO_2R/OER), the OD-Pb cathode operated in 1 M $TBABF_4$/ACN, while ultrapure water served as the anolyte. IrO_2 (Sinero), spray-coated onto Ti felt at 3 mg cm^{-2}, was used as the OER anode. A Nafion 117 membrane separated the cathode and anode compartments, and both electrolytes were circulated at 3 mL min^{-1}. Other cathode-side operating conditions were maintained comparable to those used in the CO_2R/HOR configuration.

Water-addition experiments used a 1 cm^2 OD-Pb cathode and dried electrolyte adjusted with ultrapure water to concentrations of 1, 7, 28, 55, 110, 280 or 560 mM (Supplementary Fig. 28). To assess water transport through the membrane, catholyte water accumulation in the CO_2R/OER cell was measured under open-circuit conditions and during electrolysis at 20 mA cm^{-2}, using the same cell, membrane, electrolyte and gas configuration (Supplementary Fig. 29). Water concentrations were determined by Karl Fischer titration.

Sacrificial-Zn experiments were performed in a batch cell containing 1 M $TBABF_4$/ACN. An electrodeposited Cu cathode with both sides exposed had a total exposed geometric area of 8 cm^2. A 4 cm^2 Zn plate with both sides exposed and an Ag wire served as the counter and pseudo-

reference electrodes, respectively. CO_2 was bubbled through the electrolyte at 10 mL min^{-1}. Electrolysis was conducted at 160 mA for 30 min, corresponding to 20 mA cm^{-2} based on the total exposed Cu area.

CO_2 supply experiments

CO_2 supply experiments used a 6.25 cm^2 OD-Pb cathode at 187.5 mA (30 mA cm^{-2}). Pure CO_2 flow was varied as indicated in Fig. 4a. Feed-composition experiments used 100, 70, 50, 30 or 10% CO_2 in Ar at a fixed total flow rate of 50 sccm (Supplementary Fig. 30).

For carbon-utilization measurements under a 10% CO_2 feed, the CO_2 and Ar flow rates were varied proportionally while maintaining a CO_2:Ar ratio of 1:9. CO_2 flow rates of 7, 5, 3, 2.4 and 2 sccm were paired with Ar flow rates of 63, 45, 27, 21.6 and 18 sccm, respectively.

Product analysis

Liquid products were analyzed by high-performance liquid chromatography (HPLC; LC5090PLUS, FULI INSTRUMENTS) using a PolyPak H column (5 μm, 300 mm × 7.8 mm i.d.) and UV detection at 210 nm. The mobile phase was aqueous H_2SO_4 adjusted to pH 2, supplied at 0.6 mL min^{-1}, and the column temperature was 60 °C. Oxalic and glyoxylic acids were quantified using external calibration over 0–90 and 0–35 mM, respectively.

Gaseous products were quantified by gas chromatography (GC-2014, Shimadzu) equipped with flame-ionization and thermal-conductivity detectors. Ar was used as the carrier gas for the thermal-conductivity detector. CO and H_2 were quantified by external calibration using standards of known concentrations. Cathode outlet gas flow was measured using a soap-bubble flow meter.

Physical characterization

Electrode morphology and elemental distributions were characterized by SEM–EDS (SU8220, Hitachi). Crystalline phases were identified by XRD (SmartLab 9 kW, Rigaku). Depth-resolved

ToF-SIMS measurements (M6, IONTOF) reconstructed the three-dimensional distributions of Pb, O and Fe secondary-ion signals in the PbO_2 precursor.

Radical trapping and EPR spectroscopy

DMPO was added directly to 1 M $TBABF_4$/ACN at the concentrations indicated in Fig. 2d, e, up to 50 mM. Electrolysis used OD-Pb or Cu cathodes under otherwise identical conditions, followed by HPLC and GC product quantification.

EPR samples were prepared in an H-type cell separated by Nafion 117, with 1 M $TBABF_4$/ACN in both compartments and 50 mM DMPO in the catholyte. OD-Pb and Pt mesh served as the cathode and anode, respectively. Electrolysis was conducted at 10 mA cm^{-2} (80 mA) for 1 h, after which the catholyte was immediately transferred to an EPR capillary.

Continuous-wave X-band spectra were recorded using an EPR200-Plus spectrometer (CIQTEK) at 9.8505 GHz and 2.0 mW. The magnetic field was centered at 3508.49 G with a 100 G sweep width. The modulation frequency and amplitude were 100 kHz and 1 G, respectively. Each spectrum comprised 1000 points and was averaged over two sweeps.

Online electrochemical mass spectrometry

The cathode outlet gas was monitored using a home-built EC-MS system comprising an ultrahigh-vacuum chamber and a QMA 120 quadrupole mass filter (Balzers; Supplementary Fig. 7). Full-range spectra over *m*/*z* 0–100 were collected at open circuit and during electrolysis at 20 mA cm^{-2} using Cu or OD-Pb cathodes (Supplementary Fig. 9, 18). Time-resolved signals were also recorded during stepwise changes in current density from 5 to 25 mA cm^{-2}. GC measurements independently verified the assignment of the *m/z* 28 signal to CO.

Operando Raman spectroscopy

Operando Raman spectra were acquired using a LabRAM HR Evolution microscope with a 532 nm laser. Measurements used a Cu cathode in 1 M $TBABF_4$/ACN. Spectra over 100–2200 cm^{-1} were recorded at open circuit and after 20 min of electrolysis at 5, 15, 25 or 35 mA cm^{-2}. The spectral region associated with adsorbed CO on Cu was examined (Supplementary Fig. 11).

Calculation of performance metrics

Product Faradaic efficiencies were calculated as

$$\mathrm{FE}_i = \frac{z_i\, n_i\, F}{Q} \times 100\%$$

where z_i is the electron number, n_i is the product amount, F is the Faraday constant (96485 C mol^{-1}), and Q is the charge passed. Electron numbers of 2, 4, 2, 2 and 2 were used for oxalic acid, glyoxylic acid, formic acid, CO and H_2, respectively. Total C_2 acid FE was the sum of the oxalic- and glyoxylic-acid FEs.

Liquid product amounts were calculated as $n_i = c_i V$, using HPLC concentrations and the measured post-electrolysis electrolyte volume to account for ACN evaporation. Gas product amounts were calculated as $n_i = x_i q_g t / V_m$, where x_i is the GC mole fraction, q_g is the measured outlet gas flow rate, t is the electrolysis time, and V_m is 24.5 L mol^{-1}. Compatible units were used for gas flow and time.

Single-pass carbon utilization efficiency was calculated as

$$\mathrm{SPCE} = \frac{2\left(n_{\text{oxalic acid}} + n_{\text{glyoxylic acid}}\right)}{n_{\mathrm{CO_2,in}}} \times 100\%$$

where $n_{\mathrm{CO_2,in}}$ is the amount of inlet CO_2 during the corresponding electrolysis interval, determined from the calibrated inlet flow rate, CO_2 fraction and electrolysis time.

Local CO_2 concentration simulation

Local CO_2 concentration distributions were simulated using a three-dimensional finite-element transport model in COMSOL Multiphysics (v.5.4). The geometry reproduced the experimental serpentine flow field and comprised a gas-flow channel, a 50-μm-thick porous catalyst layer and a 100-μm-thick electrolyte diffusion layer adjacent to the cathode. The model coupled gas flow, gas-phase species transport, gas-to-liquid CO_2 transfer and diffusion of dissolved CO_2, with electrochemical CO_2 consumption determined from the applied current density and experimentally measured product Faradaic efficiencies. Steady-state simulations were performed under different CO_2 flow rates and feed compositions to evaluate local CO_2 availability. Detailed governing equations and boundary conditions are provided in Supplementary Note 1.

Data availability

All data are available in the paper and the Supplementary Information. Source data that support the findings of this study are available from the corresponding authors upon reasonable request.

Acknowledgements

S.L. acknowledges NSFC (22579157), the robotic AI-Scientist platform of the Chinese Academy of Sciences, the Fundamental Research Funds for the Central Universities (WK2060250114), the Major Frontier Research Project of the University of Science and Technology of China (LS2060000002). J.Z. acknowledges support from National Key Research and Development Program of China (2021YFA1500500), CAS Project for Young Scientists in Basic Research (YSBR-051), National Natural Science Foundation of China (NSFC, 22525021, 22221003, 22250007, 22361162655), the Science and Technology Development Fund (FDCT) of Macao S.A.R (0070/2023/AFJ), Fundamental Research Funds for the Central Universities, the State Key

Laboratory of Catalysis (2024SKL-A-011), Special Science and Technology Innovation Program for Carbon Peak and Carbon Neutralization of Jiangsu Province (Grant No. BE2025014), University of Science and Technology of China-Xinjiang Normal University Counterpart Cooperation and Development Joint Fund (KY9990002504), the Key Project of Natural Science Foundation of Anhui Province (2508085ZD020), International Partnership Program of Chinese Academy of Sciences (123GJHZ2022101GC), the New Cornerstone Science Foundation through the XPLORER PRIZE. This work was partially carried out at the Instruments Center for Physical Science, University of Science and Technology of China (USTC), and USTC Center for Micro and Nanoscale Research and Fabrication. Z.Z. acknowledges National Advanced Talent Cultivation Center for Chemistry, USTC. We acknowledge the Department of Mechanical and Automation Engineering, The Chinese University of Hong Kong for the support of COMSOL simulations.

Author contributions

S.L. and J.Z. conceptualized the project, supervised the work, and provided experimental resources. Z.Z. conceived the study, designed and conducted the experiments, performed the multiphysics modeling, analyzed the data, and wrote the original draft of the manuscript. Y.Z. contributed to the electrochemical measurements. Z.W. contributed to the SEM characterization. J.Z., I.S., and S.L. contributed to scientific discussion and edited the manuscript. All authors discussed the results and assisted during manuscript preparation.

Competing interests

The authors declare that there are no known conflicts of interest associated with this work.

Additional information

Supplementary information is available in the online version of the paper.

Correspondence and requests for materials should be addressed to Shaofeng Li (shaofengli@ustc.edu.cn) and Jie Zeng (zengj@ustc.edu.cn)